ACS OMEGA

Open Access

http://pubs.acs.org/journal/acsodf

Article

Multifunctionalized Carbon Dots as an Active Nanocarrier for Drug Delivery to the Glioblastoma Cell Line

Manuel Algarra,* Juan Soto, Maria Soledad Pino-González, Elena Gonzalez-Munoz, and Tanja Dučić*

Cite This: *ACS Omega* 2024, 9, 13818−13830

Read Online

ACCESS | Metrics & More | Article Recommendations | Supporting Information

ABSTRACT: Nanoparticle-based nanocarriers represent a viable alternative to conventional direct administration in cancer cells. This advanced approach employs the use of nanotechnology to transport therapeutic agents directly to cancer cells, thereby reducing the risk of damage to healthy cells and enhancing the efficacy of treatment. By approving nanoparticle-based nanocarriers, the potential for targeted, effective treatment is greatly increased. The so-called carbon-based nanoparticles, or carbon dots, have been hydrothermally prepared and initiated by a polymerization process. We synthesized and characterized nanoparticles of 2-acrylamido-2-methylpropanesulfonic acid, which showed biocompatibility with glioblastoma cells, and further, we tested them as a carrier for the drug riluzole. The obtained nanoparticles have been extensively characterized by techniques to obtain the exact composition of their surface by using Fourier transform infrared (FTIR), X-ray photoelectron spectroscopy (XPS), and nuclear magnetic resonance (NMR) spectroscopy, as well as cryo-transmission electron microscopy. We found that the surface of the synthesized nanoparticles (NPs) is covered mainly by sulfonated, carboxylic, and substituted amide groups. These functional groups make them suitable as carriers for drug delivery in cancer cells. Specifically, we have successfully utilized the NPs as a delivery system for the drug riluzole, which has shown efficacy in treating glioblastoma cancer cells. The effect of nanoparticles as carriers for the riluzole system on glioblastoma cells was studied using live-cell synchrotron-based FTIR microspectroscopy to monitor *in situ* biochemical changes. After applying nanoparticles as nanocarriers, we have observed changes in all biomacromolecules, including the nucleic acids and protein conformation. These findings provide a strong foundation for further exploration into the development of targeted treatments for glioblastoma.

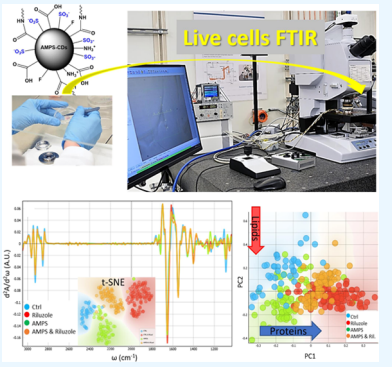

1. INTRODUCTION

The advancement of nanoscience is centered around the development of novel drug delivery systems that can effectively release drugs. This is particularly relevant given the emergence of new drug delivery carriers. As such, the primary goal of current research in this field is to devise delivery mechanisms that can enhance the efficacy and therapeutic potential of drugs.[1−5] Different carriers are developed and used because they increase the drug's power of action and overcome certain barriers to reach the cellular place of action, which improves the applied treatment. The effectiveness of the drugs is linked, in most cases, to their low solubility, in some cases to their degradation before they act, and in other more common cases, to resistance.[6] Among the systems for assumed pharmacological function, nanochemistry is currently playing a fundamental role, by developing a wide variety of nanoparticles based on a different composition.[7] A worldwide range of different particles is described in the literature for this purpose. For example, the application of gold nanoparticles and quantum dots as semiconductors at the nanoscale range[8−10] and graphene and carbon nanotubes as an alternative to inorganic nanoparticles is widely used.[11−17]

Carbon nanoparticles have received significant attention due to their abundance, eco-friendliness, aqueous solubility, diverse functionality, and biocompatibility compared to other conventional nanomaterials. These unique properties make them a promising candidate for a wide range of applications in various fields, including medicine, electronics, and environmental science. Moreover, carbon nanoparticles have shown excellent stability and durability, making them a reliable and cost-effective choice for many applications. The presence of functional groups on the surface of carbon dots (CDs), such as thiol (−SH), carboxyl (O═C−O$^-$), amine/amide (−NH_2/O═C−NH_2), and hydroxyl (−OH), provides improved physicochemical and optical properties which promote bioimaging, sensing, and drug delivery.[18−25]

Glioblastoma multiforme (GBM) is the last grade (IV) of glioma brain tumor, characterized by short median survival and the highest tumor-related mortality. Despite the increase of new chemotherapies, overall survival of patients with gliomas

Received: October 26, 2023
Revised: February 2, 2024
Accepted: February 8, 2024
Published: March 13, 2024

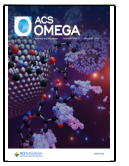

Scheme 1. Synthesis and Active Groups Depicted on the Surface of AMPS-CDs

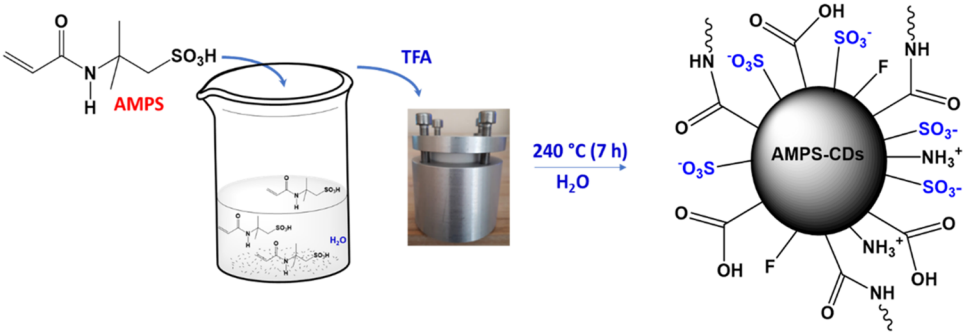

has improved only slightly.[26] Although the cellular cancer capacity for limitless proliferation depends on their genetic predisposition, the result on whether proliferation can take place depends on organic and/or elemental arrangement in cells and their environment.[27] Our previous study showed the suppressing effect of riluzole on different live patient-developed glioblastoma cell lines (GBM). Besides, riluzole directly affects biomacromolecule changes, namely, carbohydrate metabolism, DNA structure, lipid structures, and protein secondary conformation.[28] Riluzole is approved by the Food and Drug Administration (FDA) as an amyotrophic lateral sclerosis (ALS) drug,[29] and recent studies showed that treatment with riluzole suppresses the proliferation of many cancer cells[30−35] and GBM.[29,36,37] Besides, we showed that elemental composition and cytoskeletal structure differ in the same patient-derived GBM cells, as studied by synchrotron radiation-based soft-X-ray tomography and hard X-ray fluorescence.[35]

Thus, as a step forward, in this study, we first synthesized characterized and afterward tested a system based on carbon nanoparticles from the 2-acrylamido-2-methylpropanesulfonic acid (AMPS), as a possible organic delivery system (AMPS-CDs NPs), for the drug riluzole in GBM cells. We chose AMPS as a potential nanocarrier, as it possesses free sulphonyl, carboxyl, and amide groups. These groups produced the multifunctionalized surface of AMPS-CDs NPs which was first characterized. After that, their toxicity was tested on the GBM, and finally, we used them as drug delivery systems to test if they improved riluzole drug solubility and entree to cancer cells. Recently, magnetite nanoparticles grafted with poly-AMPS have been used as anionic nanoadsorbents for positively charged antibodies.[38]

Infrared (IR) spectroscopy provides highly discriminatory information due to the excitation of inherently specific fundamental vibrational transitions characteristic of molecular species[39] including nanoparticles themselves, ligands attached to the surface of NPS, and finally cellular changes. Here, we tested the effect of the synthesized AMPS-CDs NPs as a potential nanocarrier for riluzole and their effect on the biomolecules in the patient-developed glioblastoma cell line by using synchrotron radiation-based Fourier transform infrared microspectroscopy (μFTIR). We compared biochemical signatures in cells after riluzole treatment alone and after AMPS-CDs NPs treatment and compared them to control and cells treated solely with AMPS-CDs NPs. The most significant differences occurring at the level of cellular biomolecules are described in detail. Data were evaluated by statistical methods such as principal component analysis (PCA) and t-distributed stochastic neighbor embedding method (*t*-SNE) analysis. The usage of the synchrotron light as an infrared source allowed us to check the biomacromolecular signatures of single live cell levels *in situ*. The μFTIR allowed the detection of the specific metabolic changes in the intact live cell triggered by the new drug candidate nanocarrier with riluzole. To the best of our knowledge, the GBM patients' cells were still not used for live cell analysis by μFTIR spectroscopy after AMPS-CDs and riluzole simultaneous treatment.

2. MATERIALS AND METHODS

2.1. Chemicals. Carbon nanoparticles were obtained from 2-acrylamido-2-methyl-1-propanesulfonic acid (AMPS) and trifluoroacetic acid (TFA). In nuclear magnetic resonance (NMR), the solvents used were chloroform-*d* ($CDCl_3$) and methanol-d_4 (CD_3OD). All these chemicals were purchased from Sigma-Aldrich (Barcelona, Spain) and used without further manipulation. Riluzole was supplied from TOCRIS, Bio-Techne GmbH, Wiesbaden-Nordenstadt, Germany.

2.2. Synthesis of AMPS-CDs NPs. This synthesis was carried out by a facile one-step hydrothermal reaction. First, a solution of AMPS (0.131 M) was prepared with deionized Milli-Q H_2O, stirring for 30 min. From this solution, 7 mL was transferred into a 25 mL capacity Teflon-lined reactor (in-house-design), adding TFA (2 mL). The reactor was introduced into a temperature-programmed electric oven at 240 °C/7 h (Scheme 1). The purification process was carried out by a dialysis tubing cellulose membrane (Sigma-Aldrich Barcelona, Spain) *versus* H_2O. In the following scheme is depicted the synthetic hydrothermal process. Ultrapure water, used throughout all experiments, was purified through a Millipore system. All reagents were used as received without further purification.

2.3. Preparation of the Cancer Cell Samples of Human Glioblastoma in Culture. The patient-developed glioblastoma cell line (11ST) was used in this study. The cell line was primarily cultivated at the University of Medicine Göttingen, Germany, and afterward frozen, transported to the ALBA facility in a cryo-container, and grown for the experiments at the ALBA, Biology Laboratory. Ethical approval for this study was obtained from the Ethics Committee of the University Medical Center Göttingen (approval number 11/8/13). The primary cells isolated from the patient were grown in the medium containing MEM 500 mL (Gibco), 10% heat-inactivated fetal calf serum, 2 mM L-glutamine (GIBCO), 1 mM Na pyruvate (GIBCO,11360−039), and PenStrep (Thermo Fisher). Isolated cells, 4×10^4 per flask, were sped into a 25 cm^2 flask into 5 mL of medium and incubated at 37 °C and CO_2 (5%). Before data collection, cells were briefly rinsed with Ca^{2+}/Mg^{2+} free Dulbecco's phosphate-buffered

https://doi.org/10.1021/acsomega.3c08459
ACS Omega 2024, 9, 13818−13830

saline (D-PBS) and trypsinized. The cells were then seeded onto 0.5 mm thick CaF_2 windows and cultured for 24 h before measurements and treated with 50 μM riluzole, and 0.1 mg mL^{-1} AMPS-CDs alone in cell medium as well as in combination (AMPS-CDs@riluzole) for another 24 h and compared to control cells without treatment. The concentration of each component was chosen to avoid precipitation and not affect the GBM (test is shown in Figure 7). Thus, the concentration of 50 μM riluzole was chosen as the half-maximal concentration (IC_{50}; 50% of growth inhibition) of riluzole on the GBM cell lines and it was determined previously as >100 μM.[29] Here, we used the same concentration of riluzole in combination with AMPS-CDs (0.1 mg mL^{-1}), after the test, with several concentrations of AMPS-CDs. Before FTIR analysis, the morphological status of the cells was inspected to exclude dead cells (round morphology) from analysis. The fluidic device was then assembled, and the spectra were collected in the following maximal 2 h, and cells were kept at 37 °C. The complete profiling of organic compounds at the single-cell level in each case was evaluated.

2.3.1. Cell Viability Assay. Cell viability was evaluated in GBM cells by MTT assay. Briefly, GBM were plated at a density of 1×10^4 cells/well in a 96-well plate at 37 °C in a 5% CO_2 atmosphere (200 μL per well, number of replicates = 5). After 24 h, the supernatant was replaced by 200 μL/well of fresh medium with 3-[4,5-dimethylthiazol-2-yl]-2,5-diphenyl tetrazolium bromide (MTT) (0.5 mg mL^{-1}). After 2 h of incubation at 37 °C and CO_2 (5%), the medium was removed, the formazan crystals were solubilized with 200 μL of DMSO, and the solution was vigorously mixed to dissolve the reacted dye. The absorbance of each well [Abs] well was read on a microplate reader (Dynatech MR7000 instruments) at 550 nm. The relative cell viability (%) and its error relative to negative control wells containing cell culture medium without nanoparticles and positive control wells in which Triton X-100 was added to the cells were calculated by the equations

$$\mathrm{RCV}\ (\%) = (([\mathrm{Abs}]_{\mathrm{test}} - [\mathrm{Abs}]_{\mathrm{pos.ctrl.}}) / ([\mathrm{Abs}]_{\mathrm{neg.ctrl.}} - [\mathrm{Abs}]_{\mathrm{pos.ctrl.}})) \times 100$$

$$\mathrm{error}\ (\%) = \mathrm{RCV}_{\mathrm{test}} \times \mathrm{SQRT}[(\sigma_{\mathrm{test}}/[\mathrm{Abs}]_{\mathrm{test}})^2 + (\sigma_{\mathrm{test}}/[\mathrm{Abs}]_{\mathrm{test}})^2]$$

where σ is the standard deviation.

2.4. Characterization of AMPS-CDs. *2.4.1. Cryo TEM.* For cryo-transmission electron microscopy (TEM), the AMPS-CDs was diluted to a final concentration of 2 mg mL^{-1} and 3 μL of the sample was applied to glow-discharged Lacey carbon 300 mesh, blotted for 3 s (blot force −3), and frozen in liquid ethane using a Vitrobot Mark IV plunging system (Thermo Fisher Scientific). Cryo-EM grids were imaged on a Glacios microscope equipped with a Falcon 4 detector (Thermo Fisher Scientific).

2.4.2. XPS. For X-ray photoelectron spectroscopy (XPS), a Physical Electronics PHI5700 spectrometer was used using a monochromatic Mg Kα radiation of 300 W, 15 kV, and 1253.6 eV with a multichannel detector. The analysis zone was 720 μm in diameter with a path mode of 29.35 eV. The obtained spectrum was processed using the Multipak package v.9.3. To analyze the product sample, a previous dialysis and lyophilization step was needed to obtain a solid sample that could be analyzed by the XPS equipment.

2.4.3. Dynamic Light Scattering (DLS) Measurements. The ζ-potential and hydrodynamic diameter of the nanoparticles, obtained from AMPS-CDs, were determined using a Zetasizer Nano ZS (Malvern Instruments, U.K.) equipped with a 4 mW HeNe laser operating at λ = 633 nm. ζ measurements were also performed at 25 °C in folded polycarbonate capillary containers, embedded with Au-plated electrodes (DTS1061) and deionized H_2O as the dispersion medium. The values ζ were obtained automatically by applying the software of the equipment.

2.4.4. NMR Spectroscopy. The ^{1}H NMR spectra were recorded at 400 MHz, in a Bruker Advance III, and at 500 MHz, Bruker DRX 500 instruments, at the liquid NMR Service (SCAI-University of Málaga). The working frequencies used for ^{13}C were 100.6 and 125 MHz, respectively. The chemical shift values (δ) are expressed in ppm, using as internal reference the values of the chemical shifts of the solvents referred to in the TMS. The values of the coupling constants have been expressed in Hz.

2.4.5. Synchrotron Radiation-Based (SR)-FTIR Measurements. The SR-FTIR measurements were performed using a 3000 Hyperion microscope coupled to a Vertex 70v spectrometer and by using a liquid N_2-cooled mercury cadmium telluride (MCT) detector at the MIRAS beamline, at synchrotron ALBA, Barcelona, Spain. The data were collected in transmission mode using a 36× Schwarzschild objective/condenser and an aperture size of 10 μm × 10 μm. Between 44 and 105 cell spectra for each treatment were collected in the 4000−900 cm^{-1} mid-infrared range at a spectral resolution of 4 cm^{-1} with 256 coadded scans per spectrum. The live-cell device once assembled with cells and the medium was kept at 37 °C, and the spectra were collected in a period of a maximum of 2 h. For every 10 proximal individual cells, the spectrum of a buffer point was acquired with the same acquisition parameters for following water subtraction. The background was collected at the beginning of each set of measurements on the CaF_2 substrate. The synchrotron was used as the infrared light source and OPUS 8.0 (Bruker, Germany) software package for data acquisition. Spectral analysis, including the water subtraction for every single cell and second derivative (3rd polynomial order, 29 windows for smoothing points and vector normalization), was implemented. The principal component analysis (PCA) for each data set was performed, *i.e.*, after water subtraction, second derivative calculation and normalization of spectra. The PCA and *t*-SNE analysis was accomplished by using the Quasar software (Bioinformatics Laboratory of the University of Ljubljana,[40] v. 1.7.0).[41] The removal of water contributions from live cell spectra was performed by a script previously developed and described.[29] In short, the water signal on the medium close to cells was subtracted for each spectrum by using a subtraction factor from 0.8−0.95 for each cell and followed by a graphical user interface (GUI) by using the Taurus, based on the Amide I and Amide II peaks height ratio 1:0.6 (±0.1).

2.4.6. Computational Analysis. The interactions of riluzole with the surface decoration of carbon dots (SO_3^-, $-CO_2H$, NH_2-CDs $-CO_2^-$, NH_2CO-CDs) have been studied using density functional theory (DFT) with the hybrid exchange-correlation functional CAM-B3LYP[42] and the def2-SVPP basis sets[43,44] have been applied to all the atoms which form the

https://doi.org/10.1021/acsomega.3c08459
ACS Omega 2024, 9, 13818−13830

Scheme 2. Polymerization Process in the Obtention of AMPS-CDs

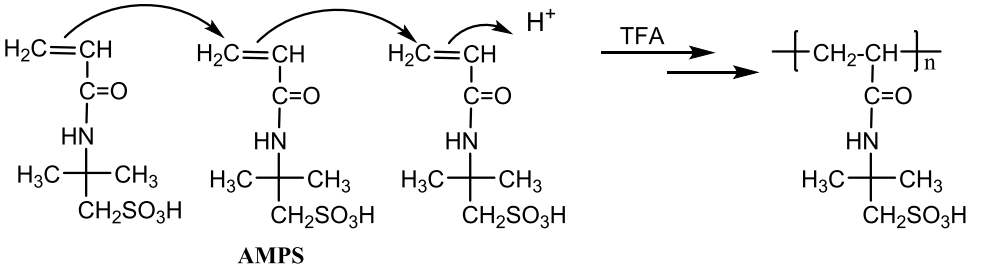

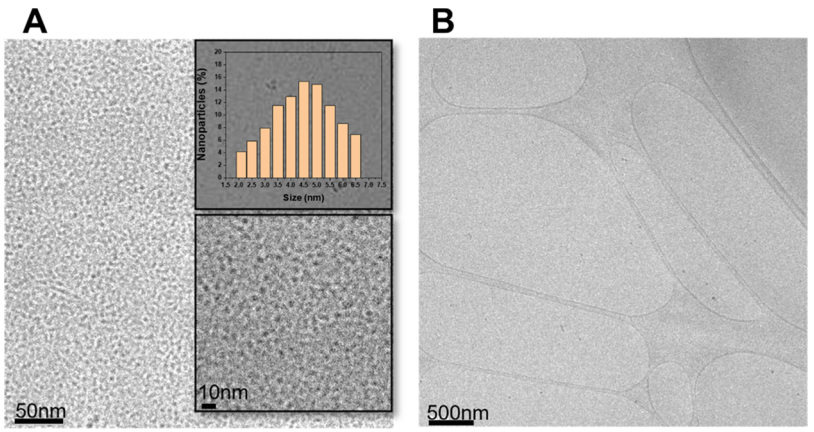

Figure 1. Cryo-TEM images of the as-obtained AMPS-CDs nanoparticles in the cell medium. The insets depicted zoom in and the histogram of the CD size. The scale is 50 nm (A) and 500 nm (B).

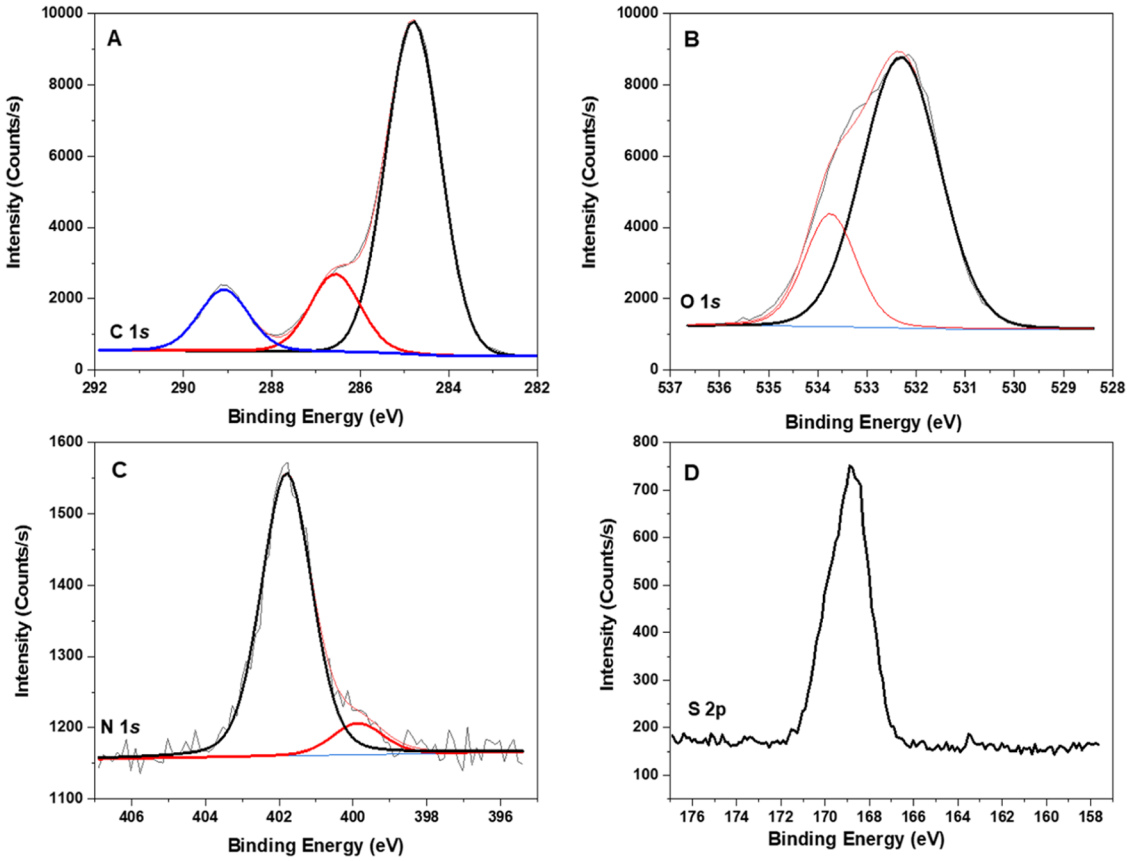

Figure 2. XPS core level spectra of (A) C 1s, (B) O 1s, (C) N 1s, and (D) S 2p of AMPS-CDs-NPs.

https://doi.org/10.1021/acsomega.3c08459
ACS Omega 2024, 9, 13818−13830

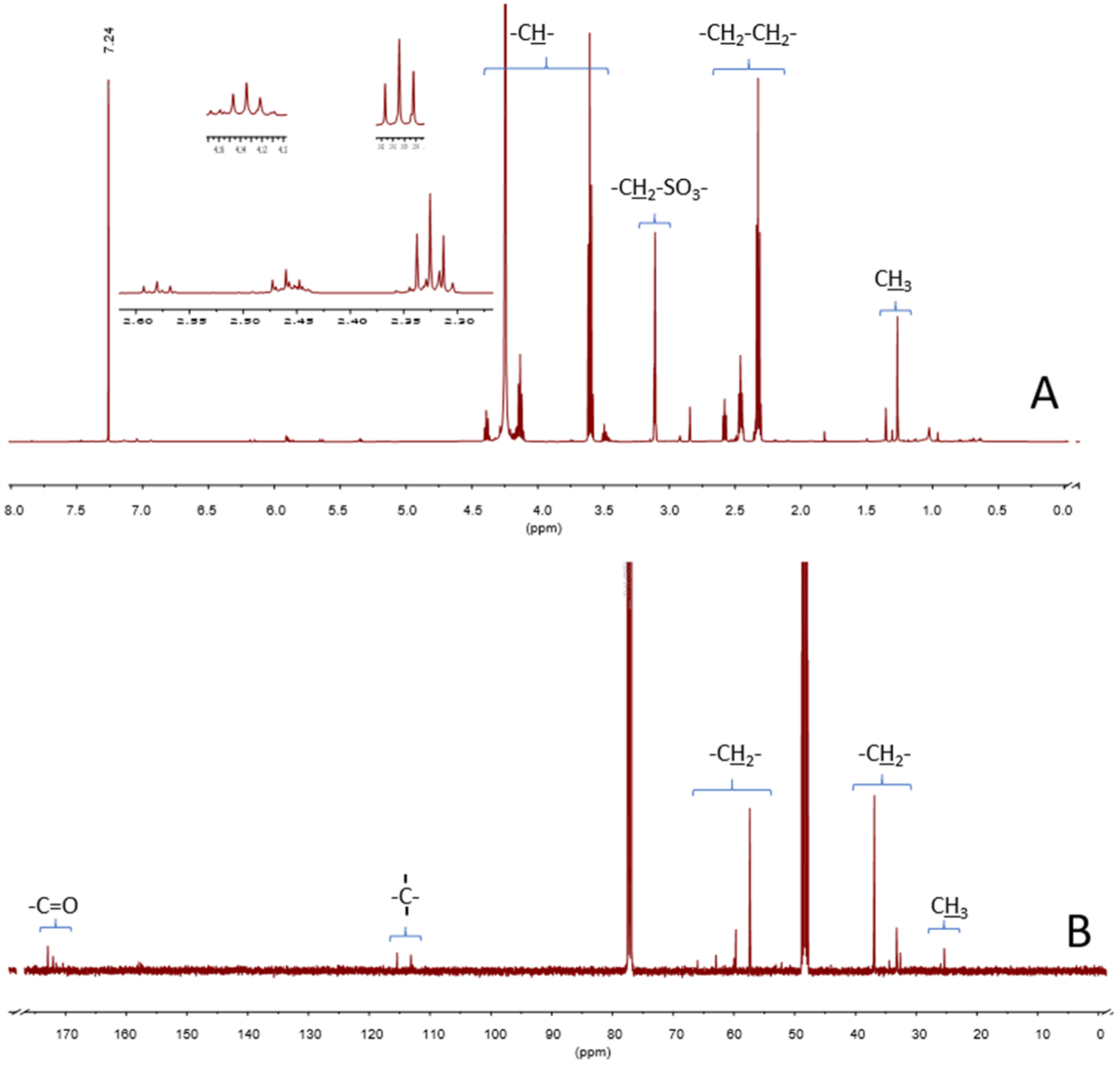

Figure 3. (A) ^{1}H NMR spectra of AMPS-CDs. (B) ^{13}C NMR spectra of AMPS-CDs. In 1:1 $CD_3OD/CDCl_3$ as solvent.

systems under study. In addition, the empirical dispersion correction of Grimme[45] has been applied on top of the optimized geometries. The electronic structure calculations were carried out with the program GAUSSIAN16.[46] Adsorption energies were determined with the standard expressions of Thermodynamics statistics. The potential energy surfaces which lead to the formation of the complexes between riluzole and AMPS-CDs have been studied using the linear interpolation method.[47−52] Molecular geometries were analyzed with the help of the MacMolPlt[53] and MOLDEN[54] graphical programs.

3. RESULTS AND DISCUSSION

The basis of the present study was to use the different methods, first, to characterize the AMPS-CDs and, second, to evaluate their effect with and without riluzole on GBM cells. Different types of tests were carried out to optimize the synthesis process of AMPS-CDs, among which the use of TFA instead of mineral acids such as sulfuric or phosphoric stands out. TFA was difficult to remove from the solution obtained, as it is an acid with moderate strength, which evaporates when the purification process is carried out; however finally, this was the best option for its preparation and further application in the cell medium. Figure SI.1 (in the Supporting Information) shows the dissolution obtained before and after irradiation under ultraviolet (UV) light with methanol and methanol/chloroform as solvents. The formation of AMPS-CDs starts with a polymerization process in the acidic media, as it is depicted in Scheme 2. This transformation is by the presence of sulfonate and -NH- groups on the surface of the AMPS-CDs, as further described by XPS. The initial polymerization leads to a subsequent conversion into properly functionalized

https://doi.org/10.1021/acsomega.3c08459
ACS Omega 2024, 9, 13818−13830

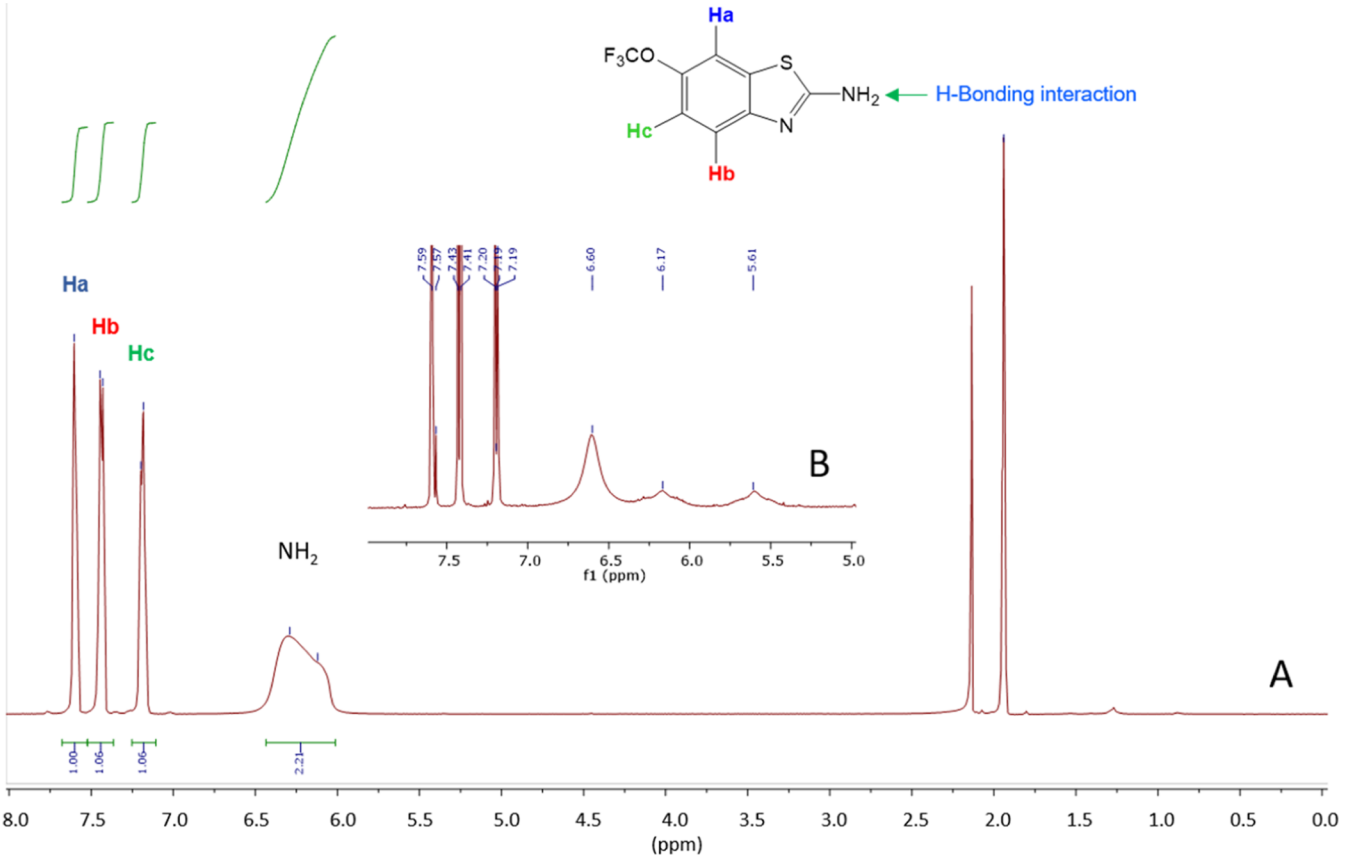

Figure 4. (A) NMR spectra of riluzole and inset (**B**) a mixture of riluzole and AMPS-CDs in CD_3CN.

carbon nanoparticles (Scheme 1), by combined effects of temperature and pressure.

3.1. Morphology and Size of AMPS-CDs. TEM analysis of AMPS-CDs showed that the nanoparticles have a medium diameter size of 4.5−5 nm (Figure 1). It is possible to observe the aggregation of the nanoparticles, with a size of ∼15 nm (Figure 1B).

3.2. Surface Analysis of AMPS-CDs. *3.2.1. XPS Analysis.* To obtain the most significant functional composition and concentration, XPS offers the best technique to characterize the surface of the obtained AMPS-CDs (Figure 2). The surface chemical concentration (in atom %) of AMPS-CDs was C, O, N, F, and S as demonstrated in the survey spectra (Figure SI.2A). The high resolution of C 1s core level spectra (Figure 2A) showed three main components, a dominant peak assigned to the C−C/C═C bonds at 284.5, at 287.5 eV to C−O/C-N, and at 289 eV for the carboxylate functional group (O−C═O) and some contribution due to C−F bonds.[55]

By the analysis of the contribution to O 1s at 532.3 and 533.3 eV, assigned to C−O/C═O, at a high binding energy, oxygen from carboxylic groups can be detected. At 533.3 eV, some surface water can also be detected. The N 1*s* core level spectrum is asymmetric due to the existence of two contributions at 399.8 and 401.7 eV (Figure 2C).[56] The high intensity can be associated with the presence of −NH− groups, in amide and amine groups as well. The latter can have been formed by degradation of the amides group.

Moreover, the contribution at high binding energy can be due to the presence of $-NH_3^+$ in alkyl ammonium groups. Based on the unique signal of the S 2p core energy level spectra (Figure 2D), the contribution at 168.7 eV is assigned to the sulfonate group (SO_3^-). These results agree with the FTIR analysis shown under in the text. Figure SI.2B depicts the F 1s core level spectra and shows a small contribution centered at 688.2 eV, which can be assigned to C−F surface bonds.

3.2.2. NMR Characterization. For NMR characterization, an attempt was made to dissolve the product obtained in an NMR tube in a 1:1 $CD_3OD/CDCl_3$ mixture, but it was not possible to solubilize most of it and a complex spectrum was obtained. The NMR tube was then placed in an ultrasound apparatus at 80W power for 20 min. The spectrum was recorded again, showing that there was a simplification of the signals concerning the initial ^1H NMR. Possibly this change is due to the destruction of aggregates, which are likely to form in an acidic medium. The most significant signals of the ^1H NMR spectrum are detailed below (Figure 3A). Several overlapping multiple-like triplets are observed, with signals centered at 4.39, 4.13, 3.60, 3.49, 2.58, 2.46, and 2.22 ppm. The correlated spectroscopy (COSY) spectra show that the signals between 2.20 and 2.60 are coupled with the signals between 3.40 and 4.50 (see Figure SI.3).

The coupling constant J = 6.2 Hz is the same for all triplets. The variation of the typical shifts for these signals could be due to a possible F-functionalization from TFA, the existence of which is verified by XPS. At 3.12 ppm, the signal corresponding to the $-CH_2$ bonded to the $-SO_3^-$ is an equation compared to the spectrum of the starting product AMPS, singlets corresponding to $C\underline{H}_3$ appear at 1.36, 1.31, and 1.27 ppm, whereas in the original molecule, the two $C\underline{H}_3$ were equivalent. In addition, the proportion of $C\underline{H}_3$ has greatly decreased compared to the rest of the signals. This could be

https://doi.org/10.1021/acsomega.3c08459
ACS Omega 2024, 9, 13818−13830

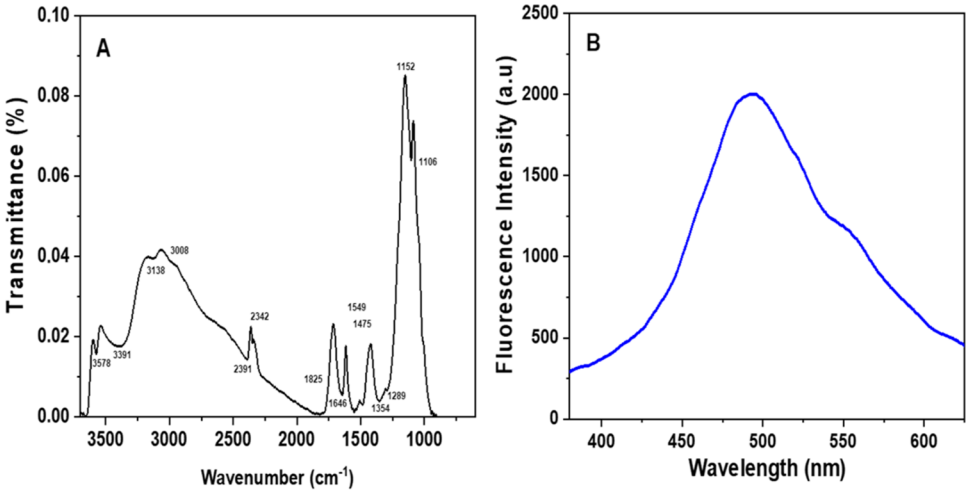

Figure 5. (A) FTIR and (B) fluorescence spectra of the AMPS-CDs NPs.

due to rearrangements on the surface of the nanoparticle upon heating.

As regards the ^{13}C NMR spectra (Figure 3B), the signals at 172.8 and 171.9 ppm correspond to the C═O group of amides. It is difficult to check by NMR whether additionally, there has been a partial hydrolysis of the amide group with the formation of amine and carboxylate groups, as shown by XPS. The signals at 115.3 and 113.0 ppm can be associated with quaternary C, as they have no correspondence in heteronuclear multiple quantum correlation (HMQC) (see Figure SI.4). Between 65.8 and 57.2 ppm and from 36.8 to 33.0 ppm, we have the $-CH_2-$ signals in the spectra. By HMQC, in addition, the $-CH_2-$ linked to $-SO_3^-$at 62.81 ppm can be distinguished, as it correlates with the signal at 3.12 ppm, already described in ^1H NMR. The signal corresponding to the methyl appears at 25.2 ppm.

To check the interaction with riluzole, we first obtained the NMR spectra of riluzole in CD_3CN and then that of the mixture with the CDs (Figure 4). It was observed that there was interaction with NH_2, varying the displacements of these two protons, from a broad signal centered at 6.25 ppm to new signals at 6.60, 6.17, and 5.61 ppm. The displacement was not total because there was a higher proportion of riluzole in the mixture. Moreover, a new signal appears at 7.57 ppm. The peaks corresponding to the rest of the AMPS-CDs did not show significant changes in the mixture.

3.2.3. FTIR Characterization of AMPS-CDs. In the FTIR spectra, (Figure 5A), is showed the stretching vibration of N−H at 3391 cm^{-1}. The presence of a strong band at 1649 cm^{-1}, from the related C═O, confirms the existence of amide groups. The band associated with the asymmetric stretching mode of the carboxylate groups appears at 1549 cm^{-1}, together with the N−H band of amide.[57] The bands of 1475/1354 cm^{-1} can be assigned to the asymmetric deformation of the CH_3 and CH_2 groups. At 1106 cm^{-1}, the S═O stretching band is enclosed, confirming the SO_3^- surface groups.[38] Moreover, the clear band at 1152 cm^{-1} is ascribed to the C−O stretching vibrations.

3.3. Optical Characterization. The fluorescence spectra (Figure 5B) showed a unique band centered at 496 nm and a small shoulder at 550 nm when excited with 325 nm. This can indicate that the process is dominated by one excited state, which corresponds mainly to the $n \rightarrow \pi^*$ transitions of the C═O and N−H groups. To corroborate this assignment, the obtained value of the parameter ζ of AMPS-CDs was negative (−11.8 mV).

This value can be explained by the presence in the surface of −COOH groups which can be deprotonated at the measured pH (pH 7). Moreover, an additional contribution in charge is due to the presence of sulfonic groups on the CD's surface.

3.4. Theoretical Analysis. *3.4.1. Structural Model.* Given that carbon dots are synthesized by attaching to the surfaces of the amorphous carbon frame, different chemical substituents are present on the surface: sulfonate SO_3^-, amine ($-NH_2$), carboxylic (−COOH), carboxylate ($-COO^-$), or ($-CONH_2$) amide groups. The doped CD models with such functionalized carbon nanoparticles chosen for studying the interaction with riluzole consist of chemical substituents bonded at one of the carbon atoms of the central ring of anthracene (Scheme 3). These structures agree with the models applied for studying analogous types of materials such as *N*-doped three-dimensional (3D)-graphene quantum dots.[58−60]

Scheme 3. CD Scheme and its Functionalized Groups Annotated with X in Possible Interaction with Riluzole

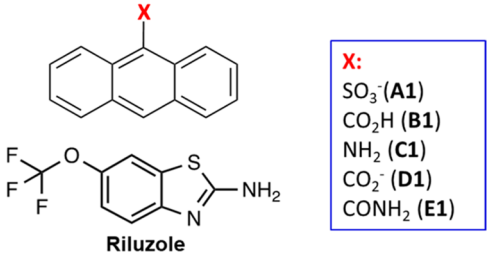

3.4.2. Interaction of AMPS-CDs with Riluzole. According to the structural models proposed in Scheme 3, the most favorable interaction of riluzole with the functional groups of AMPS-CDs NPs is calculated. The only type of interaction, after evaluation of each model, is the formation of noncovalent bonds (van der Waals bonding) between riluzole and doped carbon quantum dots whose origins are purely Coulombic and lead to the formation of AMPS-CDs@riluzole complexes without alteration of the molecular geometry of the drug,[61] which is important to keep.

https://doi.org/10.1021/acsomega.3c08459
ACS Omega 2024, 9, 13818−13830

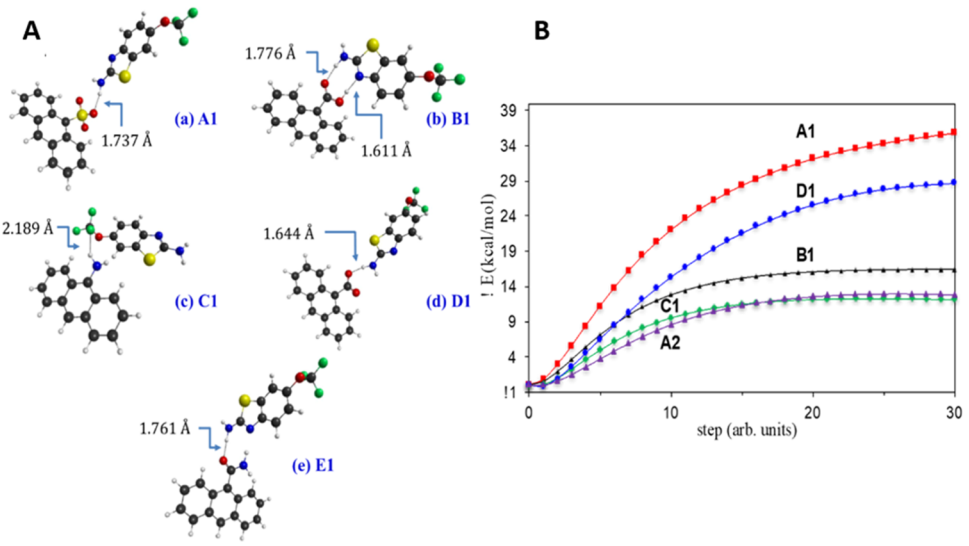

Figure 6. (A) CAM-B3LYP/def2-SVPP optimized geometries of the complexes formed between riluzole and S-CDs, C-CDs, or N-CDs. (a) **A1** ($-SO_3^-$); (b) **B1** (−COOH); (c) **C1** ($-NH_2$); (d) **D1** ($-COO^-$); (e) **E1** ($-CH_2NH_2$). (**B**) CAM-B3LYP/def2-TSVPP potential energy surfaces (relative electronic energy in kcal mol^{-1}) of the complexes formed between riluzole and N-CDs or S-CDs. (**A**) **A1** ($-SO_3^-$); (**B**) **B1** (−COOH); (**C**) **C1** ($-NH_2$); (**D**) **D1** ($-COO^-$); (**E**) **E1** ($-CONH_2$).

The minimum energy geometries of such complexes are represented in Figure 6A, and Table 1 shows their reaction enthalpies (Δ_rH) and Gibbs free energies (Δ_rG) computed at 298.15 K, as well as the electronic energies of the reactions. The most stable complexes correspond to the interaction between the $-NH_2$ group in riluzole and SO_3^- (**A1**) or $-COO^-$ (**E1**) groups in AMPS-CDs, whose functional groups are charged, respectively. The potential energy surfaces that lead to the formation of each molecular complex obtained with the linear interpolation method are presented in Figure 6B.[48−51] Such interpolations indicate that the potential surfaces for the complex formation are barrierless, *i.e.*, the AMPS-CDs NPs act as attractors. The −NH-bonding interactions belonging to $-NH_2$ from riluzole can be observed in Figure 6, **A1**, **B1**, **D1**, and **E1**, verifying the interactions shown in NMR spectra (Figure 4B).

Table 1. CAM-B3LYP/def2-SVPP(D3)//CAM-B3LYP/def2-SVPP Reaction Enthalpies and Gibbs Free Energies for Formation of AMPS-CDs@riluzole Complexes[a]

complex[b]	Δ_rE_e[c]	Δ_rH	Δ_rG
A1	−29.0	−27.7	−17.6
B1	−25.3	−24.2	−12.7
C1	−8.8	−7.4	+1.6
D1	−33.9	−32.7	−22.4
E1	−21.0	−19.4	−8.2

[a]Temperature: 298.15 K; energies in kcal mol^{-1}. [b]Geometries given in Figure 6. [c]Electronic energy in kcal mol^{-1}.

3.5. AMPS-CDs as a Nanocarrier for Riluzole Drug (AMPS-CDs@riluzole) Affect the Glioblastoma Cells.

Previously, we showed that 50 μM riluzole was the optimal concentration to influence live GBM cells as a concentration within the scale of the maximum tolerated dose of 100 μM in medical practice and as it has already shown a promising effect on cell lines *in vitro* as well as *in vivo* CAM assay.[29] To examine the effect of riluzole alone and in combination with AMPS-CDs NPs, the glioblastoma cell line was incubated with 50 μM riluzole, and 0.1 mg mL^{-1} AMPS-CDs NPs alone and in

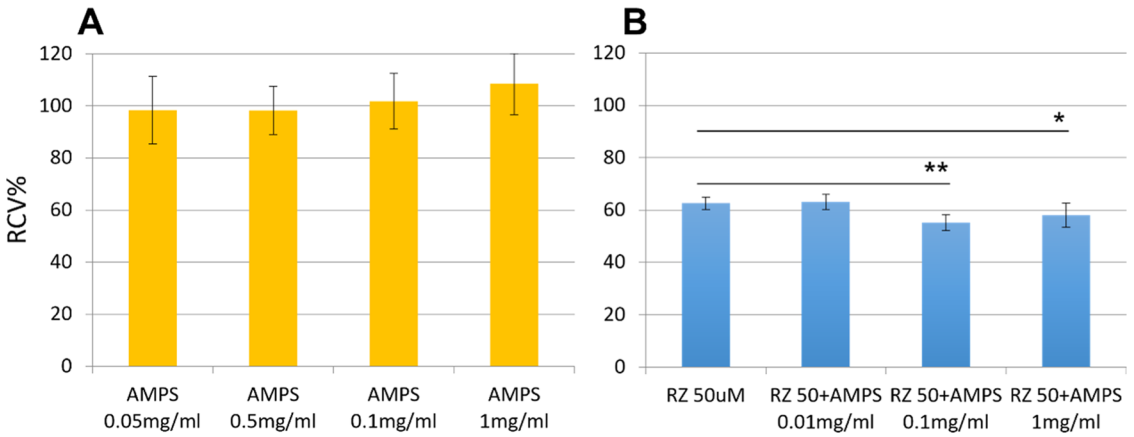

Figure 7. (A) Relative cell viability after treatment with AMPS-CDs NPs in different concentrations on the GBM 11ST cell line and (B) AMPS-CDs@riluzole. *$p \leq 0.05$, **$p \leq 0.01$ when compared with cells treated with 50 μM riluzole by the *t*-test.

https://doi.org/10.1021/acsomega.3c08459
ACS Omega 2024, 9, 13818−13830

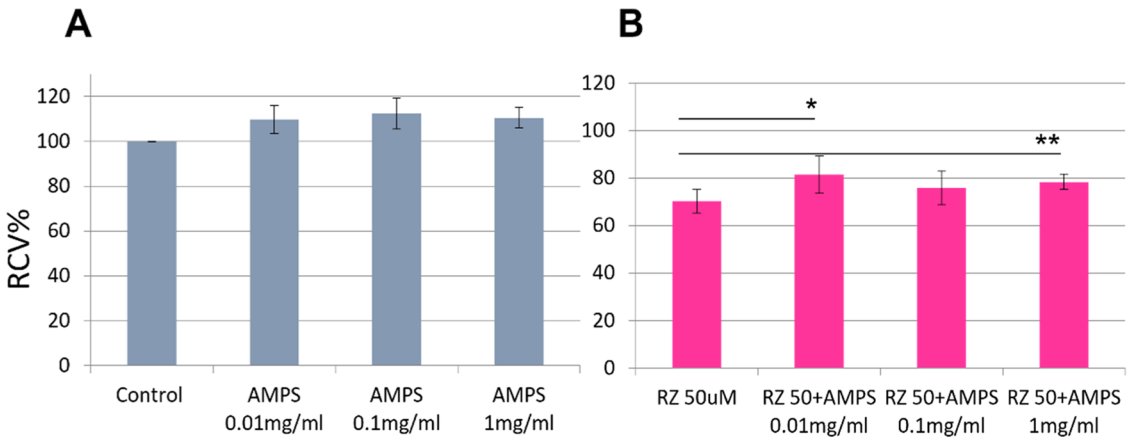

Figure 8. (A) Relative cell viability of healthy human astrocytes after treatment with AMPS-CDs NPs in different concentrations on astrocytes cell line P10251 and (B) AMPS-CDs@riluzole. $*p \leq 0.05$, $**p \leq 0.01$ when compared with the cells treated with 50 μM riluzole by the *t*-test.

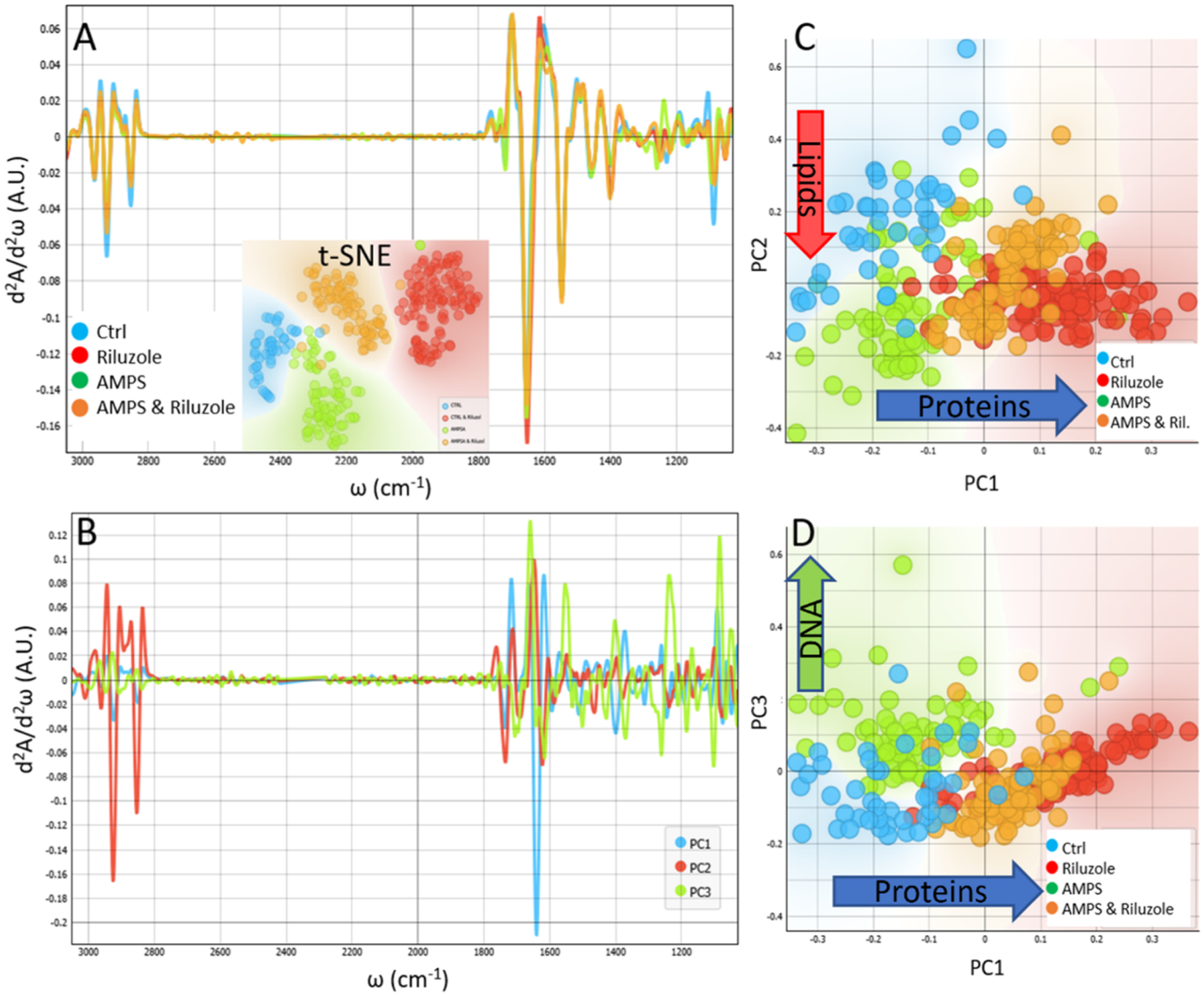

Figure 9. (A) The second derivate of the FTIR averaged spectra of live 11ST cells grown in the cell medium (blue), after treatment of riluzole (red), after treatment with AMPS-CDs NPs (green) and AMPS-CDs@riluzole (orange) in the spectral region of the lipids, 3100−1030 cm^{-1}. Insets show the *t*-SNE analysis. (B) PCAs (loading values) of the first three principal components PC1 (blue), PC2 (red), and PC3 (green) showing the contribution of individual absorbance of corresponding areas in the graphs above shown in (C and D). $N = 44-105$.

https://doi.org/10.1021/acsomega.3c08459
ACS Omega 2024, 9, 13818−13830

combination for 24 h and after that, submitted for the FTIR spectrum collection in the live cells setup. The live-cell FTIR measurement was employed to study the effect of the AMPS-CDs NPs as a nanocarrier for the riluzole drug on the most important bioorganic molecules, such as proteins, lipids, nucleic acids, and carbohydrates. In this study, essential biomacromolecules were evaluated in the live cells without any invasive cell preparation.

First, the cytotoxic effect was performed on the primary glioblastoma cells isolated from patient 11ST for the potential effect of the riluzole drug alone and with the AMPS-CDs nanocarrier. The AMPS-CDs NPs did not show a cytotoxic effect on the cells, even in relatively high concentrations gently increasing cell viability (Figure 7A). The optimal concentration of AMPS-CDs NPs and riluzole for treating cells was evaluated, as the concentration has the greatest impact on GBM (data not shown). Here, we focused on the effect of 50 μM riluzole as we have previously shown it to be close to the IC_{50} concentration and have proven the molecular and survival impact on live GBM cells.[29] It is shown that a combination of 50 μM riluzole and 0.1 mg mL^{-1} AMPS-CD has significantly lowered cell viability ($p \leq 0.01$), while higher concentration of the CDs showed less effect (Figure 7B).

Besides, we analyze the effect of the AMPS-CDs NPs and riluzole on the cell viability of nontumor human astrocytes (provided by Innoprot, Derio, Spain, ref P10251 Human astrocytes) (Figure 8). As expected, AMPS-CDs did not affect cell viability with a tendency to increase it (nonsignificant). However, interestingly, the combination of AMPS-CDs with riluzole significantly increased cell viability compared to the treatment with riluzole alone (Figure 8B), showing an opposite effect to that occurring in GBM tumor cells. This different effect was specifically evident after the cells were treated with the 50 μM riluzole and 0.1 mg mL^{-1} AMPS-CD combination as it causes the highest significant GBM mortality (Figure 7B). Tumor GBM cells show a 55 ± 3% of cell viability, while survival of nontumor astrocytes increased to 76 ± 7% (Figure 8B). The fact that CDs had a positive effect on healthy astrocyte cells even at low concentrations makes it appealing to hypothesize that this drug and nanocarrier combination presents a promising effect on cancer cells, which would have minimal effect on the healthy cells and deserve further investigation.

3.6. Live Cell FTIR Assay on the GBM Treated with AMPS-CDs as a Nanocarrier for Riluzole Drug (AMPS-CDs@riluzole). As a continuation of our previous study with different synchrotron light-based X-ray techniques on the same GBM cells, we explored the changes in most cells' crucial biomacromolecules after treatment with riluzole and AMPS-CDs NPs by using SR-FTIR for GMB live cell analysis.[29] The analysis of various metabolic molecules was conducted within live cells in a controlled physiological environment and constant temperature of 37 °C. The results, depicted in Figure 9A, clearly demonstrate the efficacy of this method. Figure 9 presents the main biomacromolecule FTIR signatures of the 11ST cell lines in live conditions. After applying water correction to each spectrum of individual cell measurements (N = 44−105) and vector normalization, a second derivative analysis was carried out. The comparison of main spectral bands, which represent lipids, proteins, esters, carbohydrates, and nucleic acids, was performed using the average spectra as presented in Figure 9A. The analysis of single-cell FTIR signatures using t-SNE based on their second derivative average spectra across all spectral ranges resulted in distinct separation of the measured groups, as demonstrated in the inset in Figure 9A. To further identify specific differences, we conducted PCA analysis and plotted the loading of the first three principal components, as illustrated in Figure 8B. As can be observed, the first principal component (PC1) displayed the most differences in the protein's area (blue arrow in Figure 9C,D shows orientation), while PC2 was prominent in the lipid's areas (red arrow in Figure 9C), and PC3 in the nucleic acids area, mostly DNA (green arrow in Figure 9D). The plotted PCs, PC1 and PC2, and PC1 and PC3 in Figure 9C,D, respectively, clearly exhibited the segregation of all measured groups. The PCA score demonstrated that segregation occurred mostly over the PC1, which highlighted the distinctions in the secondary protein structure. Based on the loading plots, it appears that PC1 (represented by the blue line) exhibits the most notable discrepancies at approximately 1644 cm^{-1}, pointing to the random coil protein structure that is more prominent in cells treated with riluzole. On the other hand, a favorable impact on the control and AMPS-CDs cells can be observed around 1717 cm^{-1} (carboxyl group) and 1620 cm^{-1} (associated with β-structure and free amino acid chains). Regarding the lipid region, the primary differences are observed in the bands located at roughly 2926 and 2853 cm^{-1}, which are assigned to $\nu_{as}CH_2$ and $\nu_{s}CH_2$,[62,63] respectively. These bands associate with log acyl chains in lipids, which were lower in riluzole and riluzole and AMPS-CDs NPs treatments when compared to the control and only AMPS-CDs NPs treatment (PC2). This indicates possible lipid peroxidation processes which occur in riluzole and CD treatments.[64] In the fingerprint area (1480−1030 cm^{-1}), the phosphate bands predominantly exhibited considerable differences. The control cells demonstrated higher absorbances at 1087/1235 cm^{-1}, which were related to phosphate symmetric and asymmetric stretching vibration, respectively.[64] These were higher in the only AMPS-CDs NPs treated cells.

Although the AMPS-CDs nanoparticles themselves were not toxic, when combined with riluzole, they had a positive impact on promoting cell death on GBM. These results indicate that AMPS-CD nanoparticles could potentially serve as a carrier for riluzole in the treatment of glioblastoma cancer cells. Pairing of riluzole and AMPS-CDs nanoparticles had a advantageous effect on changes in nucleic acids and accordingly protein conformations in GBM. Specifically, the nanoparticles caused a shift in protein structure, leading to an increase in α-helix structure (at 1656 cm^{-1}) in the cells. Further research on noncancerous cells may provide a more comprehensive understanding of the nanoparticles' overall effects.

4. CONCLUSIONS

Our study aimed to create new safe AMPS-CDs and test them on live cells isolated from a patient's glioblastoma cell line. We used the AMPS-CDs@riluzole system and observed the cell viability in cancer and noncancerous cells, as well as to follow the changes in the biomacromolecule profile of GBM cells, including the emergence of random coil protein structures. This suggests that the effects of the system are not limited to DNA, but also extend to protein conformation. This is a promising finding and indicates that AMPS-CDs could be a useful nanocarrier for delivering riluzole and targeting proteins in glioblastoma cancer cells.

https://doi.org/10.1021/acsomega.3c08459
ACS Omega 2024, 9, 13818−13830

■ ASSOCIATED CONTENT

Supporting Information

The Supporting Information is available free of charge at https://pubs.acs.org/doi/10.1021/acsomega.3c08459.

AMPS-CDs solution under vis light and UV light; AMPS-CDs XPS: (A) survey; (B) F 1s core level spectra; COSY-NMR spectra in $CDCl_3$-MeOD 1:1; HMQC-NMR spectra in $CDCl_3$-MeOD 1:1; FTIR spectra of AMPS, riluzole, and AMPS-CDs@riluzole (PDF)

■ AUTHOR INFORMATION

Corresponding Authors

Manuel Algarra − *INAMAT²—Institute for Advanced Materials and Mathematics, Dept. Science, Public University of Navarra, 31006 Pamplona, Spain;* orcid.org/0000-0003-2410-8430; Email: manuel.algarra@unavarra.es

Tanja Dučić − *ALBA-CELLS Synchrotron Light Source, Consorcio para la Construccion Equipamiento y Explotacion del Laboratorio de Luz Sincrotron, 08290 Cerdanyola del Vallès, Barcelona, Spain;* orcid.org/0000-0003-2389-3887; Email: tducic@cells.es

Authors

Juan Soto − *Dept. Physical Chemistry, Faculty of Science, University of Málaga, 29071 Málaga, Spain;* orcid.org/0000-0001-6702-2878

Maria Soledad Pino-González − *Dept. Organic Chemistry, Faculty of Science, University of Málaga, 29071 Málaga, Spain;* orcid.org/0000-0001-7711-6771

Elena Gonzalez-Munoz − *Instituto de Investigación Biomédica de Málaga y Plataforma en Nanomedicina-IBIMA Plataforma BIONAND., 29590 Málaga, Spain; Dept. Cell Biology, Genetics and Physiology, University of Málaga, 29071 Málaga, Spain;* orcid.org/0000-0001-8291-1518

Complete contact information is available at: https://pubs.acs.org/10.1021/acsomega.3c08459

Author Contributions

Conceptualization: T.D. and M.A.; investigation: T.D., J.S., M.S.P.-G., E.G.-M., and M.A.; formal analysis: T.D., J.S., M.S.P.-G., M.A., and E.G.-M.; visualization: T.D., J.S., and M.S.P.-G.; writing—original draft: T.D. and M.A.; writing—review and editing: all authors. All authors read and approved the final manuscript.

Notes

The authors declare no competing financial interest.

■ ACKNOWLEDGMENTS

The authors are grateful for financial support from the Spanish Ministry of Science and Innovation (MCIN/AEI/10.13039/501100011033) through project PID2021-122613OB-I00 as well as the ALBA In-house grant: "Synergetic multimodal FTIR and X-ray spectro-microscopical approach for 3D cell culture evaluation". Open access funding is provided by Universidad Pública de Navarra. The authors are grateful to Professor Veit Rohde, Dr. Milena Ninkovic, and Swetlana Sperling, Department of Neurosurgery, University Medical Center Göttingen, Germany, for cell providing and support for the cell culturing. The authors thank Dr. Pablo Guerra from the IBMB-CSIC CryoEM Platform for assistance during the sample preparation and microscope data acquisition. The authors acknowledge funding from Project, IU16-014045 (CRYO-TEM) from Generalitat de Catalunya and by "ERDF A way of making Europe", by the European Union. The authors are thankful to Dragoljub Dimitrijevic for assistance during the spectroscopical measurements. JS thanks R. Larrosa and D. Guerrero for the technical support in running the calculations and the SCBI (Supercomputer and Bioinformatics) center of the University of Málaga for computer resources.

■ REFERENCES

(1) Huang, X.; Wu, S.; Du, X. Gated mesoporous carbon nanoparticles as drug delivery system for stimuli-responsive controlled release. *Carbon* **2016**, *101*, 135−142.

(2) Webber, M. J.; Langer, R. Drug delivery by supramolecular design. *Chem. Soc. Rev.* **2017**, *46*, 6600−6620.

(3) Elsharkasy, O. M.; Nordin, J. Z.; Hagey, D. W.; de Jong, O. G.; Schiffelers, R. M.; EL Andaloussi, S.; Vader, P. Extracellular vesicles as drug delivery systems: Why and how? *Adv. Drug Delivery Rev.* **2020**, *159*, 332−343.

(4) Han, C.; Zhang, X.; Wang, F.; Yu, Q.; Chen, F.; Shen, D.; Yang, Z.; Wang, T.; Jiang, M.; Deng, T.; Yu, C. Duplex metal co-doped carbon quantum dots-based drug delivery system with intelligent adjustable size as an adjuvant for synergistic cancer therapy. *Carbon* **2021**, *183*, 789−808.

(5) Anand, A.; Jian, H. J.; Huang, H. H.; Hean, L. E.; Li, Y. J.; Lai, J. Y.; Chou, H. D.; Kang, Y. C.; Wu, W. C.; Lai, C. C.; Huang, C. C.; Chang, H. T. Anti-angiogenic carbon nanovesicles loaded with bevacizumab for the treatment of age-related macular degeneration. *Carbon* **2023**, *201*, 362−370.

(6) Patra, J. K.; Das, G.; Fraceto, L. F.; Campos, E. V. R.; Rodríguez-Torres, M. D. P.; Acosta-Torres, L. S.; Díaz-Torres, L. A.; Grillo, R.; Swamy, M. K.; Sharma, S.; Habtemariam, S.; Shin, H. S. Nano-based drug delivery systems: recent developments and prospects. *J. Nanobiotechnol.* **2018**, *16*, No. 71, DOI: 10.1186/s12951-018-0392-8.

(7) Han, S. P.; Kim, J. H.; Han, M. E.; Sim, H. E.; Kim, K. S.; Yoon, S.; Baek, S. Y.; Kim, B. S.; Oh, S. O. SNAI1 Is Involved in the Proliferation and Migration of Glioblastoma Cells. *Cell. Mol. Neurobiol.* **2011**, *31*, 489−496.

(8) Paris, J. L.; Baeza, A.; Vallet-Regí, M. Overcoming the stability, toxicity, and biodegradation challenges of tumor stimuli-responsive inorganic nanoparticles for delivery of cancer therapeutics. *Expert Opin. Drug Delivery* **2019**, *16*, 1095−1112.

(9) Kong, F. Y.; Zhang, J. W.; Li, R. F.; Wang, Z. X.; Wang, W. J.; Wang, W. Unique Roles of Gold Nanoparticles in Drug Delivery, Targeting and Imaging Applications. *Molecules* **2017**, *22*, No. 1445, DOI: 10.3390/molecules22091445.

(10) Lungu, I. I.; Holban, A. M.; Grumezescu, A. M. Superiorities of Nanoscale Materials in Drug Delivery. In *Materials for Biomedical Engineering*; Holban, A. M.; Grumezescu, A. M., Eds.; Elsevier, 2019; pp 1−18.

(11) Abdelhamid, H. N.; El-Bery, H. M.; Metwally, A. A.; Elshazly, M.; Hathout, R. M. Synthesis of CdS-modified chitosan quantum dots for the drug delivery of Sesamol. Carbohydr. *Polymer* **2019**, *214*, 90−99.

(12) Han, X.; Huang, J.; Lin, H.; Wang, Z.; Li, P.; Chen, Y. 2D Ultrathin MXene-Based Drug-Delivery Nanoplatform for Synergistic Photothermal Ablation and Chemotherapy of Cancer. *Adv. Healthcare Mater.* **2018**, *7*, No. 1701394, DOI: 10.1002/adhm.201701394.

(13) Liu, A.; Liu, Y.; Liu, G.; Zhang, A.; Cheng, Y.; Li, Y.; Zhang, L.; Wang, L.; Zhou, H.; Liu, J.; Wang, H. Engineering of surface modified $Ti_3C_2T_x$ MXene based dually controlled drug release system for synergistic multitherapies of cancer. *Chem. Eng. J.* **2022**, *448*, No. 137691.

(14) Zamhuri, A.; Lim, G. P.; Ma, N. L.; et al. MXene in the lens of biomedical engineering: synthesis, applications and future outlook. *BioMed. Eng. Online* **2021**, *20*, No. 33, DOI: 10.1186/s12938-021-00873-9.

(15) Iravani, S.; Varma, R. S. MXenes and MXene-based materials for tissue engineering and regenerative medicine: recent advances. *Mater. Adv.* **2021**, *2*, 2906−2917.
(16) Hoseini-Ghahfarokhi, M.; Mirkiani, S.; Mozaffari, N.; Sadatlu, M. A. A.; Ghasemi, A.; Abbaspour, S.; Akbarian, M.; Farjadian, F.; Karimi M, M. Applications of Graphene and Graphene Oxide in Smart Drug/Gene Delivery: Is the World Still Flat? *Int. J. Nanomed.* **2020**, *15*, 9469−9496.
(17) Campbell, E.; Hasan, M. T.; Pho, C.; Callaghan, K.; Akkaraju, G. R.; Naumov, A. V. Graphene Oxide as a Multifunctional Platform for Intracellular Delivery, Imaging, and Cancer Sensing. *Sci. Rep.* **2019**, *9*, No. 416.
(18) Biju, V. Chemical modifications and bioconjugate reactions of nanomaterials for sensing, imaging, drug delivery and therapy. *Chem. Soc. Rev.* **2014**, *43*, 744−764.
(19) Travlou, N. A.; Giannakoudakis, D. A.; Algarra, M.; Labella, A. M.; Rodríguez-Castellon, E.; Bandosz, T. J. S and N-doped carbon quantum dots: Surface chemistry dependent antibacterial activity. *Carbon* **2018**, *135*, 104−111.
(20) Du, J.; Xu, N.; Fan, J.; Sun, W.; Peng, X. Carbon Dots for In Vivo Bioimaging and Theranostics. *Small* **2019**, *15*, No. 1805087.
(21) Liu, J.; Li, R.; Yang, B. Carbon Dots: A New Type of Carbon-Based Nanomaterial with Wide Applications. *ACS Cent. Sci.* **2020**, *6*, 2179−2195.
(22) Wareing, T. C.; Gentile, P.; Phan, A. N. Biomass-Based Carbon Dots: Current Development and Future Perspectives. *ACS Nano* **2021**, *15*, 15471−15501.
(23) Calabrese, G.; De Luca, G.; Nocito, G.; Rizzo, M. G.; Lombardo, S. P.; Chisari, G.; Forte, S.; Sciuto, E. L.; Conoci, S. Carbon dots: An Innovative tool for drug delivery in brain tumors. *Int. J. Mol. Sci.* **2021**, *22*, No. 11783, DOI: 10.3390/ijms222111783.
(24) Zhu, P.; Wang, S.; Zhang, Y.; Li, Y.; Liu, Y.; Li, W.; Wang, Y.; Yan, X.; Luo, D. Carbon Dots in Biomedicine: A Review. *ACS Appl. Bio Mater.* **2022**, *5*, 2031−2045.
(25) Crista, D.; Algarra, M.; de Yuso, M. V. M.; da Silva, J. C. G. E.; da Silva, L. P. Investigation of the role of pH and the stoichiometry of the N-dopant in the luminescence, composition, and synthesis yield of carbon dots. *J. Mater. Chem. B* **2023**, *11*, 1131−1143, DOI: 10.1039/D2TB02318K.
(26) *Advances in Nanotechnology-Based Drug Delivery Systems*; Das Talukdar, A.; Sarker, S. D.; Patra, J. K., Eds.; Elsevier, 2022.
(27) Welsh, C. T. Molecular Mechanisms of Pathogenesis and Current Therapeutic Strategies. In *Glioblastoma*; Ray, S. K., Ed.; Springer, 2010.
(28) Han, S. P.; Kim, J. H.; Han, M. E.; Sim, H. E.; Kim, K. S.; Yoon, S.; Baek, S. Y.; Kim, B. S.; Oh, S. O. SNAI1 Is Involved in the Proliferation and Migration of Glioblastoma Cells. *Cell. Mol. Neurobiol.* **2011**, *31*, 489−496.
(29) Dučić, T.; Ninković, M.; Martínez-Rovira, I.; Sperling, S.; Rohde, V.; Dimitrijević, D.; Jover Mañas, G. V.; Vaccari, L.; Birarda, G.; Yousef, I. Live-Cell Synchrotron-Based FTIR Evaluation of Metabolic Compounds in Brain Glioblastoma Cell Lines after Riluzole Treatment. *Anal. Chem.* **2022**, *94*, 1932−1940.
(30) Sperling, S.; Aung, T.; Martin, S.; Rohde, V.; Ninkovic, M. Riluzole: A Potential Therapeutic Intervention in Human Brain Tumor Stem-like Cells. *Oncotarget* **2017**, *8*, 96697−96709.
(31) Liu, J.; Wang, L. N. The efficacy and safety of riluzole for neurodegenerative movement disorders: a systematic review with meta-analysis. *Drug Delivery* **2018**, *25*, 43−48.
(32) Armando, R.; Gómez, D. M.; Gómez, D. New drugs are not enough-drug repositioning in oncology: An update. *Int. J. Oncol.* **2020**, *56*, 651−684, DOI: 10.3892/ijo.2020.4966.
(33) Lemieszek, M. K.; Stepulak, A.; Sawa-Wejksza, K.; Czerwonka, A.; Ikonomidou, C.; Rzeski, W. Riluzole Inhibits Proliferation, Migration and Cell Cycle Progression and Induces Apoptosis in Tumor Cells of Various Origins. *Anti-cancer Agents Med. Chem.* **2018**, *18*, 565−572.
(34) Blyufer, A.; Lhamo, S.; Tam, C.; Tariq, I.; Thavornwatanayong, T.; Mahajan, S. S. Riluzole: A neuroprotective drug with potential as a novel anti-cancer agent. *Int. J. Oncol.* **2021**, *59*, No. 95, DOI: 10.3892/ijo.2021.5275.
(35) Dučić, T.; Paunesku, T.; Chen, S.; Ninković, M.; Speling, S.; Wilke, C.; Lai, B.; Woloschak, G. Structural and elemental changes in glioblastoma cells in situ: complementary imaging with high-resolution visible light- and X-ray microscopy. *Analyst* **2017**, *142*, 356−365.
(36) Yelskaya, Z.; Carrillo, V.; Dubisz, E.; Gulzar, H.; Morgan, D.; Mahajan, S. S. Synergistic Inhibition of Survival, Proliferation, and Migration of U87 Cells with a Combination of LY341495 and Iressa. *PLoS One* **2013**, *8*, No. e64588, DOI: 10.1371/journal.pone.0064588.
(37) Sachkova, A.; Sperling, S.; Mielke, D.; Schatlo, B.; Rohde, V.; Ninkovic, M. Combined Applications of Repurposed Drugs and Their Detrimental Effects on Glioblastoma Cells. *Anticancer Res.* **2019**, *39*, 207−214.
(38) Inthanusorn, W.; Rutnakornpituk, M.; Rutnakornpituk, B. Reusable poly(2-acrylamido-2-methylpropanesulfonic acid)-grafted magnetic nanoparticles as anionic nano-adsorbents for antibody and antigen. *Int. J. Polym. Mater. Polym. Biomater.* **2023**, *72*, 636−645.
(39) López-Lorente, Á. I.; Mizaikoff, B. Recent advances on the characterization of nanoparticles using infrared spectroscopy. *TrAC, Trends Anal. Chem.* **2016**, *84*, 97−106.
(40) Demšar, J.; Curk, T.; Erjavec, A.; Gorup, Č.; Hočevar, T.; Milutinovič, M.; Možina, M.; Polajnar, M.; Toplak, M.; Starič, A.; Štajdohar, M.; Umek, L.; Žagar, L.; Žbontar, J.; Žitnik, M.; Zupan, B. Orange: Data mining toolbox in Python. *J. Mach. Learn. Res.* **2013**, *14*, 2349−2353.
(41) Toplak, M.; Birarda, G.; Read, S.; Sandt, C.; Rosendahl, S. M.; Vaccari, L.; Demšar, J.; Borondics, F. Infrared Orange: Connecting Hyperspectral Data with Machine Learning. *Synchrotron Radiat. News* **2017**, *30*, 40−45.
(42) Yanai, T.; Tew, D.; Handy, N. A new hybrid exchange-correlation functional using the Coulomb-attenuating method (CAM-B3LYP). *Chem. Phys. Lett.* **2004**, *393*, 51−57.
(43) Weigend, F.; Ahlrichs, R. Balanced basis sets of split valence, triple zeta valence and quadruple zeta valence quality for H to Rn: Design and assessment of accuracy. *Phys. Chem. Chem. Phys.* **2005**, *7*, 3297−3305.
(44) Weigend, F. Accurate Coulomb-fitting basis sets for H to Rn. *Phys. Chem. Chem. Phys.* **2006**, *8*, 1057−1065.
(45) Grimme, S.; Antony, J.; Ehrlich, S.; Krieg, H. A consistent and accurate ab initio parameterization of density functional dispersion correction (DFT-D) for the 94 elements H-Pu. *J. Chem. Phys.* **2010**, *132*, No. 154104, DOI: 10.1063/1.3382344.
(46) Frisch, M. J.; Trucks, G. W.; Schlegel, H. B.; Scuseria, G. E.; Robb, M. A.; Cheeseman, J. R.; Scalmani, G.; Barone, V.; Petersson, G. A.; Nakatsuji, H.; Li, X.; Caricato, M.; Marenich, A. V.; Bloino, J.; Janesko, B. G.; Gomperts, R.; Mennucci, B.; Hratchian, H. P.; Ortiz, J. V.; Izmaylov, A. F.; Sonnenberg, J. L.; Williams-Young, D.; Ding, F.; Lipparini, F.; Egidi, F.; Goings, J.; Peng, B.; Petrone, A.; Henderson, T.; Ranasinghe, D.; Zakrzewski, V. G.; Gao, J.; Rega, N.; Zheng, G.; Liang, W.; Hada, M.; Ehara, M.; Toyota, K.; Fukuda, R.; Hasegawa, J.; Ishida, M.; Nakajima, T.; Honda, Y.; Kitao, O.; Nakai, H.; Vreven, T.; Throssell, K.; Montgomery, J. A., Jr.; Peralta, J. E.; Ogliaro, F.; Bearpark, M. J.; Heyd, J. J.; Brothers, E. N.; Kudin, K. N.; Staroverov, V. N.; Keith, T. A.; Kobayashi, R.; Normand, J.; Raghavachari, K.; Rendell, A. P.; Burant, J. C.; Iyengar, S. S.; Tomasi, J.; Cossi, M.; Millam, J. M.; Klene, M.; Adamo, C.; Cammi, R.; Ochterski, J. W.; Martin, R. L.; Morokuma, K.; Farkas, O.; Foresman, J. B.; Fox, D. J. *Gaussian 16 Revision A.03*; Gaussian, Inc.: Wallingford CT, 2016.
(47) Algarra, M.; Soto, J. Insights into the Thermal and Photochemical Reaction Mechanisms of Azidoacetonitrile. Spectroscopic and MS-CASPT2 Calculations. *ChemPhysChem* **2020**, *21*, 1126−1133.
(48) Soto, J.; Algarra, M. Electronic Structure of Nitrobenzene: A Benchmark Example of the Accuracy of the Multi-State CASPT2 Theory. *J. Phys. Chem. A* **2021**, *125*, 9431−9437.
(49) Nunes, N.; Popović, I.; Abreu, E.; Maciel, D.; Rodrigues, J.; Soto, J.; Algarra, M.; Petković, M. Detection of Ru potential

https://doi.org/10.1021/acsomega.3c08459
ACS Omega 2024, 9, 13818−13830

metallodrug in human urine by MALDI-TOF mass spectrometry: Validation and options to enhance the sensitivity. *Talanta* **2021**, *222*, No. 121551, DOI: 10.1016/j.talanta.2020.121551.
(50) Soto, J.; Peláez, D.; Otero, J. C. A SA-CASSCF and MS-CASPT2 study on the electronic structure of nitrosobenzene and its relation to its dissociation dynamics. *J. Chem. Phys.* **2021**, *154*, No. 044307.
(51) Soto, J.; Peláez, D.; Otero, J. C.; Ávila, F. J.; Arenas, J. F. Photodissociation Mechanism of Methyl Nitrate. A study with the Multistate Second-Order Multiconfigurational Perturbation Theory. *Phys. Chem. Chem. Phys.* **2009**, *11*, 2631−2639.
(52) Soto, J.; Algarra, M.; Peláez, D. Nitrene formation is the first step of the thermal and photochemical decomposition reactions of organic azides. *Phys. Chem. Chem. Phys.* **2022**, *24*, 5109−5115.
(53) Bode, B. M.; Gordon, M. S. MacMolPlt: A graphical user interface for GAMESS. *J. Mol. Graphics Modell.* **1998**, *16*, 133−138.
(54) Schaftenaar, G.; Noordik, J. H. MOLDEN: a pre- and post-processing program for molecular and electronic structures. *J. Comput. Aided Mol. Des.* **2000**, *14*, 123−134.
(55) Zhao, F. G.; Zhao, G.; Liu, X. H.; Ge, C. W.; Wang, J. T.; Li, B. L.; Wang, Q. G.; Li, W. S.; Chen, Q. Y. Fluorinated graphene: Facile solution preparation and tailorable properties by fluorine-content tuning. *J. Mater. Chem. A* **2014**, *2*, 8782−8789.
(56) Moulder, J. F.; Stickle, W. F.; Sobol, P. E.; Bomben, K. D. *Handbook of X Ray Photoelectron Spectroscopy: A Reference Book of Standard Spectra for Identification and Interpretation of XPS Data*; Physical Electronics,Inc., 1995.
(57) Mecozzi, M.; Sturchio, E. Computer Assisted Examination of Infrared and Near Infrared Spectra to Assess Structural and Molecular Changes in Biological Samples Exposed to Pollutants: A Case of Study. *J. Imaging* **2017**, *3*, No. 11, DOI: 10.3390/jimaging3010011.
(58) Algarra, M.; Moreno, V.; Lazaro-Martinez, J. M.; Rodriguez-Castellon, E.; Soto, J.; Morales, J.; Benítez, A. Insights into the formation of N doped 3D-graphene quantum dots. Spectroscopic and computational approach. *J. Colloid Interface Sci.* **2020**, *561*, 678−686.
(59) Louleb, M.; Latrous, L.; Ríos, A.; Zougagh, M.; Rodríguez-Castellón, E.; Algarra, M.; Soto, J. Detection of Dopamine in human fluids using N-doped carbon dots. *ACS Appl. Nano Mater.* **2020**, *3*, 8004−8011.
(60) Houdová, D.; Soto, J.; Castro, R.; Rodrigues, J.; Pino-González, M. S.; Petković, M.; Bandosz, T. J.; Algarra, M. Chemically heterogeneous carbon dots enhanced cholesterol detection by MALDI TOF mass spectrometry. *J. Colloid Interface Sci.* **2021**, *591*, 373−383.
(61) Dučić, T.; Alves, C. S.; Vučinić, Ž.; Lázaro-Martínez, J. M.; Petković, M.; Soto, J.; Mutavdžić, D.; Martínez de Yuso, M. V.; Radotić, K.; Algarra, M. S, *N*-doped carbon dots-based cisplatin delivery system in adenocarcinoma cells: Spectroscopical and computational approach. *J. Colloid Interface Sci.* **2022**, *623*, 226−237.
(62) Clark, T.; Murray, J. S.; Politzer, P. A perspective on quantum mechanics and chemical concepts in describing noncovalent interactions. *Phys. Chem. Chem. Phys.* **2018**, *20*, 30076−30082.
(63) Nešić, M. D.; Dučić, T.; Gonçalves, M.; Stepić, M.; Algarra, M.; Soto, J.; Gemović, B.; Bandosz, T. J.; Petković, M. Biochemical changes in cancer cells induced by photoactive nanosystem based on carbon dots loaded with Ru-complex. *Chem. Biol. Interact.* **2022**, *360*, No. 109950.
(64) Malek, K.; Wood, B. R.; Bambery, K. R. FTIR Imaging of Tissues: Techniques and Methods of Analysis. In *Optical Spectroscopy and Computational Methods in Biology and Medicine*; Springer Netherlands: Dordrecht, 2014; pp 419−473.

https://doi.org/10.1021/acsomega.3c08459
ACS Omega 2024, 9, 13818−13830